

Advances in Microscale Laser Shock Peening*

CHEN Hongqiang, WANG Youneng, KYSAR Jeffrey W., YAO Y. Lawrence**

Department of Mechanical Engineering, Columbia University, New York 10027, USA

Abstract: The response of materials after microscale laser shock peening (μ LSP) was experimentally characterized and compared with the theoretical prediction from the finite element method (FEM) analysis in microlength level. X-ray micro-diffraction technique was applied to the post-peened single crystal aluminum of (001) and (110) orientations, and X-ray profile was analyzed by sub-profiling and Fourier analysis method. Spatially resolved residual stress and strain deviation was quantified and explained in terms of the heterogeneous dislocation cell structure. In-plane crystal lattice rotation induced by μ LSP was measured by electron backscatter diffraction (EBSD) and compared with the FEM simulation. Average mosaic size was evaluated from X-ray profile Fourier analysis and compared with the result from EBSD. Surface strength increase and dislocation cell structure formation were studied. The systematical characterization will lay the ground work for better understanding the effect of μ LSP in microlength level and developing more realistic simulations.

Key words: laser shock peening; X-ray micro-diffraction; single crystal

Introduction

In recent decades, failure and reliability of microelectro-mechanical systems (MEMS) have been drawing increasing attention^[1, 2]. Fatigue behavior, for instance, may ultimately limit product lifetime in certain applications, such as microengines and microswitches. Needs will arise to impart a desirable residual stress distribution or alter the existing distribution left by the fabrication process itself. Microscale laser shock peening (μ LSP) is a technique that can potentially be applied to manipulate the residual stress distribution in surface layers of metal structures with micron-level spatial resolution and thus enhance fatigue and reliability performances of microdevices^[3].

Microscale laser shock processing of polycrystalline aluminum and copper has been studied and shown to significantly improve fatigue performance of the peened targets due to the compressive residual stress^[4-6]. It has also been shown through the finite element method (FEM) simulation results that the microscale laser shock peening (LSP) efficiently induces favorable residual stress distributions in metal targets. To fully understand the effect of μ LSP and validate the FEM result, it is always desirable to measure directly the residual stress distribution after μ LSP. Conventional X-ray diffraction (Cu-K α X-ray source) was used to measure average residual stress/strain in the depth direction for overlapping shock processed bulk copper sample^[4]. However, the spatial resolution of normal X-ray diffraction is typically larger than 0.5 mm, which is too large to measure the residual stress/strain distributions in microscale laser shock peening^[5]. Recently, by using synchrotron radiation sources, X-ray microdiffraction measurements based on intensity contrast method^[7,8] provide the possibility of measuring the region of stress/strain concentration with

Received: 2004-07-05

* Supported by the National Science Foundation of USA (No. DMI-02-00334) and the National Science Foundation of USA under the Faculty Early Career Development (CAREER) Program (No. CMS-0134226)

** To whom correspondence should be addressed.
E-mail: ylyl@columbia.edu; Tel: 1-(212)854-2887
Fax: 1-(212)854-3304

micron-level spatial resolution in copper thin-film samples by recording the diffraction intensity contrast of the underlying single crystal silicon substrate^[6]. The result provides useful information about the strain field distribution in shock processed copper films, but it is difficult to relate the X-ray diffraction intensity contrast with the stress/strain values quantitatively and it is an indirect measurement since the diffraction signal was taken from the silicon substrate and not from the copper thin film itself.

The mechanics of laser shock peening presents many exciting challenges because it is a hybrid process involving many disciplines. However, classical solid continuum mechanics is hard to explain plastic deformation confined to the micron length scale^[9]. Thus, to comprehensively model the whole process, micromechanical considerations and their relationship to crystal structure, crystal lattice orientation, dislocation, and other microstructures under shock wave require careful study. Transmission electron microscopy (TEM) observations of the microstructure of the shock area were carried out to understand the response to laser shock peening at micron-level^[10,11]. However, peened samples need to be cut to very thin slices for TEM observation and the experimental results cannot quantitatively characterize the microstructure of the shocked area. Thus, new characterization methods need to be developed to quantitatively measure the microstructure caused by μ LSP.

In this paper, the spatially resolved X-ray diffraction profiles from microscale laser shock peened bulk single crystal aluminum of different crystalline orientations (001 and 110) were recorded at the microscale. The spatial distributions of residual stress/strain, strain deviation, and mosaic size induced in microscale laser shock peening were experimentally quantified by X-ray microdiffraction. Crystal lattice rotation caused by plastic deformation during high-strain rate laser shock peening was measured by electron backscatter diffraction (EBSD). The experimental results were then compared with that of simulations obtained from FEM analysis based on single crystal plasticity. Thus, these measurements provide the possibility to study the response of materials to laser shock peening at the microscale and can be used to verify the results of FEM analysis as well. Also, the experiments and FEM analysis provide new methods for characterizing the

microstructure formation and distribution of plastic deformation for microscale laser shock peening.

1 Experiment and Simulation Conditions

1.1 Laser shock peening experiment conditions

As illustrated in Fig. 1, a frequency tripled Q-switched Nd: YAG laser ($\lambda = 355$ nm) in the TEM₀₀ mode was used in the laser shock peening. The pulse duration was 50 ns, spacing between consecutive pulses along a shock line was 25 μ m, and pulse numbers were 3 on each shocked location at 1 kHz pulse repetition rate. Laser beam diameter was 12 μ m and laser intensity was approximately 4 GW/cm². A thin layer of high vacuum grease (about 10 μ m thick) was spread evenly on the polished sample surface, and a 16- μ m thick polycrystalline aluminum foil, chosen for its relatively low threshold of vaporization, was tightly pressed onto the grease. The sample was placed in a shallow container filled with distilled water around 3 mm above the sample's top surface. After shock processing, the coating layer and the vacuum grease were manually removed. The induced deformation is due to shock pressure and not due to thermal effects since only the coating is vaporized by the laser shock. Further details of microscale LSP setup are given in Refs. [4-6].

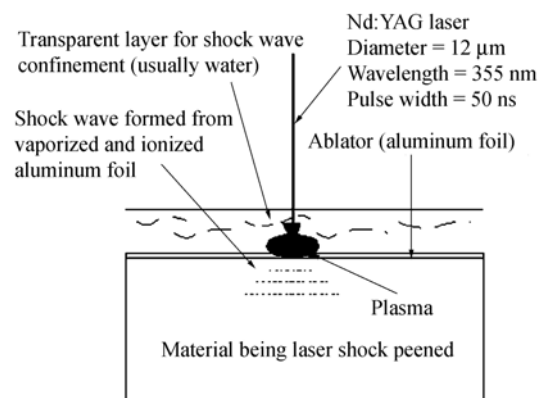


Fig. 1 Laser shock peening process

Fully-annealed single crystals of pure aluminum with orientations (001) and (110), shown in Fig. 2, were used for μ LSP here since aluminum is one of materials that routinely used in microdevices due to its good mechanical and electrical properties. Although polycrystalline metals are more widely used in practice, single crystal metal is ideal for fundamental study. The

sample was cut to shape using a wire electrical discharge machining (EDM). Laue pattern X-ray was used to determine the crystal orientation within $\pm 1^\circ$ and LSP was applied along this direction in all samples. Regular mechanical polishing with diamond grit sizes $6\ \mu\text{m}$ and $1\ \mu\text{m}$ was used to remove the heat-affected zone of the cutting surface and electrochemical polishing was applied for all samples to eliminate any remaining deformed material prior to shock peening.

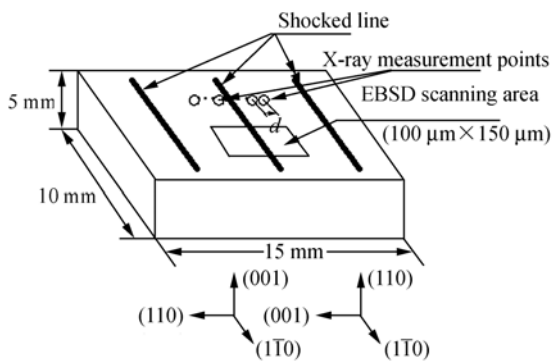


Fig. 2 Sample geometry and laser shock peening condition (X-ray measurement points are along a line perpendicular to a shocked line and within $\pm 100\ \mu\text{m}$ from the center of that shocked line, $d=5\ \mu\text{m}$; within $\pm 20\ \mu\text{m}$ from the shocked line center, $d=10\ \mu\text{m}$, elsewhere. EBSD scan area is $100\ \mu\text{m} \times 150\ \mu\text{m}$).

1.2 FEM simulation conditions

In the FEM analysis, the spatial and temporal dependent shock pressure was solved numerically based on Ref. [12] and was extended to a spatial nonuniform shock pressure with a Gaussian spatial distribution. The non-uniform shock pressure was then used as the loading for the subsequent stress/strain analysis. A commercial FEM code, ABAQUS, is used for the stress/strain analysis as a two-step quasi-static loading and unloading process corresponding to the shock peening and relaxation processes. Based on the theory of Asaro^[13], a user-material subroutine called UMAT for single crystal plasticity written by Huang^[14] and modified by Kysar^[15] is incorporated into the finite element analysis^[16]. In the UMAT, the $\{111\}\langle 110\rangle$ slip systems in face-centered cubic (FCC) metal are used for single crystal Al.

A critical shear strength $\tau_{\text{CRSS}}=1\ \text{MPa}$ on each of the slip systems is assumed. Simulation was carried out assuming finite geometry ($800\ \mu\text{m}$ in length and $400\ \mu\text{m}$ in height). Shocks are applied to the top surface along

a narrow strip in the width direction. The bottom surface is fixed in position, while all the other side surfaces are set traction free. In order to eliminate the “volume-locking” that occurs in plastic deformation simulation, linear elements with reduced integration and hourglass stiffness control are used. With the FEM model based on single crystal plasticity, material response at either macroscale or microscale can be predicted, such as geometry deformation, residual stress/strain spatial distribution, and lattice rotation field, etc. Figures 3 and 4 show the typical simulation results about strain distributions in sample surface and lattice rotation field on cross section for sample Al (001) and Al (110). However, it is necessary to verify the predications and optimize parameters of FEM model by experiments both in macro and micro levels.

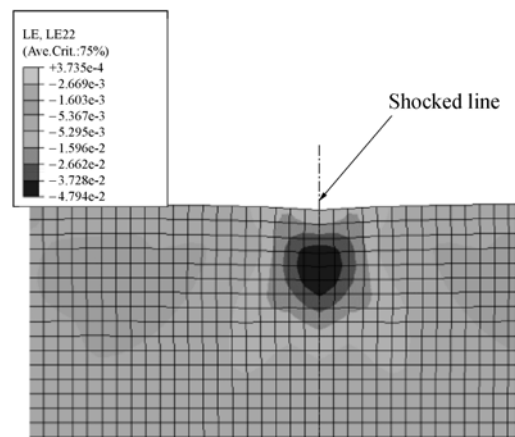


Fig. 3 Typical FEM simulation result of strain distribution in depth direction, Al (001) sample: $200\ \mu\text{m} \times 80\ \mu\text{m}$ as shown, total simulation region is $800\ \mu\text{m} \times 400\ \mu\text{m}$, and deformation factor is 5 for viewing clarity.

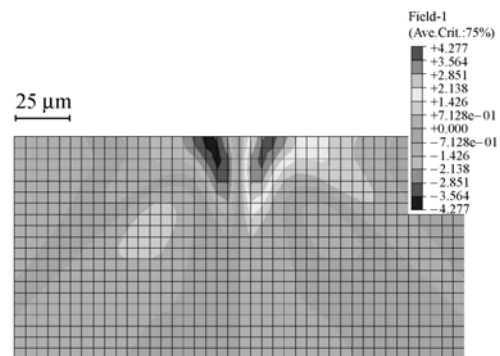


Fig. 4 Typical lattice rotation field on cross section after LSP, Al (110) sample: $200\ \mu\text{m} \times 100\ \mu\text{m}$ as shown, total simulation region is $800\ \mu\text{m} \times 400\ \mu\text{m}$.

2 Measurement and Characterization Methods

2.1 X-ray microdiffraction measurement

A high brightness X-ray beam (beamline X20A) of National Synchrotron Light Source at Brookhaven National Lab was used in diffraction and the beam size was $5\ \mu\text{m} \times 7\ \mu\text{m}$. Monochromatic synchrotron radiation at 8.0 keV ($\lambda=0.154\ 024\ \text{nm}$) is used, since it is smaller than the K absorption edge for Al and Cu which are 8.98 keV and 8.3 keV^[17] so that the fluorescence radiation would not be excited. To obtain proper 2θ diffraction profile for each measurement point, the diffraction conditions of θ and χ angles should be optimized for every measuring point. That is, the optimization of the two Euler angles, θ and χ , is to set the normal of the diffracting planes at the proper orientation on the diffractometer^[18].

Multiple measurement points are chosen along a line perpendicular to a shocked line as shown in Fig. 2. The spacing between adjacent measurement points starts from $10\ \mu\text{m}$ (when $\pm 100\ \mu\text{m}$ away from the center of the shocked line) and reduces to $5\ \mu\text{m}$ within $\pm 20\ \mu\text{m}$ from the center of the shocked line to spatially resolve the residual stress, as shown in Fig. 2. At each position, the corresponding X-ray diffraction profile is recorded by a modified version of the SPEC software package^[19] and repeated for each shocked line.

2.2 EBSD measurement

In addition to X-ray microdiffraction, electron backscatter diffraction (EBSD), a technique for obtaining crystallographic orientation with sub-micron spatial resolution was applied to the shock peened samples. Microstructure changes, such as crystallographic orientation and texture, were studied quantitatively. EBSD data was collected using a system supplied by HKL Technology^[20] and attached to a JEOL JSM 5600LV scanning electron microscope. The samples were briefly electrically polished to remove the mechanical scratches on the surface. The shocked region was accurately located using SEM before the EBSD measurements. All data were acquired in the automatic mode, using external beam scanning and employing a $1\text{-}\mu\text{m}$ step size. The scan area is $100\ \mu\text{m} \times 150\ \mu\text{m}$ on the shocked surface and covered the shocked line center as

shown in Fig. 2. Details about EBSD measurement can be found in Ref. [21].

2.3 Spatially resolved residual strain/stress evaluation method

If a piece of metal is deformed elastically such that the strain is uniform over a relatively large distance, the uniform macrostrain will cause a shift in the diffraction lines to new positions. If the metal is deformed plastically, such as in this case, the deformation creates adjacent regions of slight different orientations. The residual strain can vary from region to region to cause non-homogeneous strain state, which results in strain deviation and a broadening of the diffraction profile. In fact, both kinds of strains are superposed in plastically deformed metals, and diffraction is both shifted and broadened^[17]. It is the superposition that makes it difficult to evaluate the local strain and residual stress distribution.

However, on the basis of a composite model, local strain and residual stress can be evaluated for single crystal metal under plastic deformation as reported by Ungar^[22] by recognizing that the crystal dislocations often arrange themselves in a cell structure. A cell structure consists of “cell interiors” and “cell wall” as postulated by Ref. [22]. The cell walls parallel to the compressive axis are under a residual uniaxial compressive stress $\Delta\sigma_w < 0$ and the cell interior under a uniaxial tensile stress $\Delta\sigma_c > 0$. The asymmetrical Bragg reflections can then be separated into the sum of two symmetrical peaks which correspond to “cell interiors” and “cell wall”. For brevity, the subscripts w and c will be used for walls and cell interiors. The integral intensities of the sub-profiles relative to the integral intensity of the measured profile are proportional to the volume fractions of the cell walls f_w and cell interiors $f_c = 1 - f_w$, respectively. According to the model, stress equilibrium of the unloaded crystal requires

$$f_w \Delta\sigma_w + (1 - f_w) \Delta\sigma_c = 0 \quad (1)$$

The asymmetric line profiles I are assumed to be composed of two components I_w and I_c , where I_w is attributed to the cell-wall material (the integral intensity of which is proportional to f_w) and I_c to the cell-interior material (the integral intensity of I_c is proportional to $f_c = 1 - f_w$). The centers of both components are shifted in opposite directions in accordance with $\Delta\sigma_w < 0$ and $\Delta\sigma_c > 0$. These shifts can be expressed by the relative

change of the mean lattice plane spacing $\Delta d/d$ as follows:

$$\left. \frac{\Delta d}{d} \right|_w = \frac{\Delta \sigma_w}{E} < 0, \quad \left. \frac{\Delta d}{d} \right|_c = \frac{\Delta \sigma_c}{E} > 0 \quad (2)$$

where E is Young modulus. We introduce a Cartesian coordinate system with the z -axis parallel to the stress axis and the x - and y -axes perpendicular to the two sets of walls that are parallel to the stress axis. Then, the measure of the residual stresses can be characterized by the absolute value of the difference,

$$\sigma_{zz} = |\Delta \sigma_w - \Delta \sigma_c| \quad (3)$$

Their range of influence is of the order of the cell dimensions, which is longer than the range of individual dislocations in a random distribution, e.g., in cell walls or in cell interiors. The lateral residual stress in the sample surface plane is

$$\sigma_{xx} = \sigma_{yy} = -\sigma_{zz} \nu \quad (4)$$

where ν denotes the Poisson ratio.

2.4 Strain deviation and mosaic size evaluation method

Based on the Fourier analysis of the diffraction profiles, the Warren and Averbach method^[23] allows to obtain strain deviation and distribution function of mosaic size directly from the Fourier series coefficients.

Considering a single crystal sample in which there is a plastic deformation induced by laser shock peening, there is a non-uniform spacing change between the diffraction planes in a region and the strain variation is thus induced, causing a broadening of X-ray line profile. The shock peening also produces dislocation arrays^[22, 24], such as small angle boundaries which subdivide the original single crystal into small coherent domains as grains in polygrained metal. As a result, the peened region can be regarded as polygrained metal^[25]. Those small mosaics-like grains will cause the broadening of line profile since there are not as many planes to cause destructive interference away from the exact Bragg angle^[17]. Therefore, both kinds of effects contribute to the broadening of the X-ray line profile in plastically deformed metals.

From the analysis of Ref. [23], the sample can be represented as columns of unit cells along the direction which is perpendicular to the diffraction plane in the reciprocal lattice space. The X-ray line profile can be

considered as the combination of reflected X-ray from all pairs of unit cells. The measured X-ray line profile is then represented as the Fourier series in the reciprocal lattice space^[23]

$$P(2\theta) = \frac{KNF^2}{\sin^2 \theta} \sum_{n=-\infty}^{+\infty} (A_n \cos 2\pi nh + B_n \sin 2\pi nh) \quad (5)$$

where $P(2\theta)$ represents the measured X-ray line profile vs. 2θ , F is the structure factor and K is the angular factor. N represents the number of unit cells in the sample and h is the reciprocal of the lattice spacing. The real part of Fourier coefficient A_n can be described as the product of the size effect and the strain effect^[26]:

$$A_n = A_n^S A_n^D \quad (6)$$

where A_n^D represents the spacing change between the diffraction planes and A_n^S is a measure of the grain size. Furthermore, for small values of l and n , A_n can be expressed by Ref. [26]:

$$\ln A_n = \ln A_n^S - 2\pi^2 l^2 n^2 \langle \varepsilon^2 \rangle \quad (7)$$

where l is the number of unit cells between diffraction planes and $\langle \varepsilon^2 \rangle^{1/2}$ is the standard strain deviation which indicates strain uncertainty. According to Eq. (7), $\ln A_n$ vs. n^2 is represented as a straight line, whose slope and intersection with $n=0$ can be used to evaluate the strain deviation and size effects.

3 Results and Discussions

As mentioned above, after shock peening, macroscopic quantities (residual strain and stress) and microscopic quantities (crystalline orientation field, mosaic size, etc.) can be evaluated with the analysis method based on the data from X-ray microdiffraction or EBSD measurement in Sections 2.1 and 2.2, and compared with the FEM simulation.

3.1 Macroscopic quantities

3.1.1 Spatially resolved residual stress characterization

Figures 5 and 6 show the three-dimensional spatial distribution of those measured X-ray profiles for Al (002) and (220) reflection in the direction perpendicular to the shocked line, respectively. The corresponding X-ray profiles at shock peened center and unshocked region are shown in Figs. 7 and 8. It is clear that after

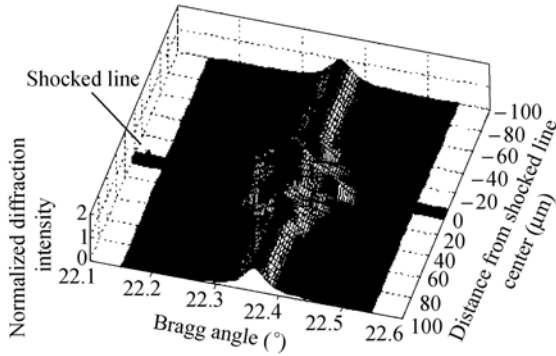


Fig. 5 3-D X-ray profile spatial distribution across the shocked line for (002) reflection of Al (001) sample^[24]

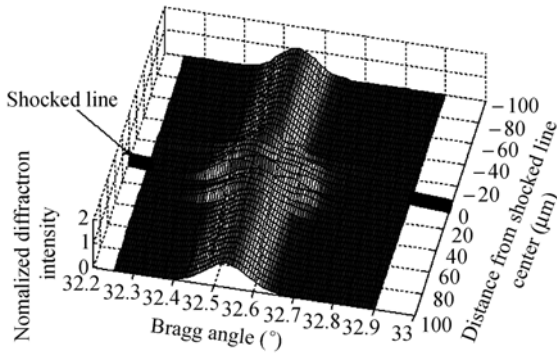


Fig. 6 3-D X-ray profile spatial distribution across the shocked line for (220) reflection of Al (110) sample

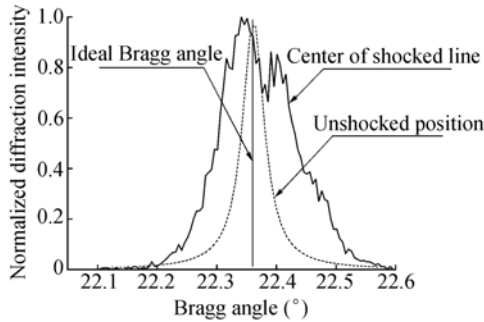


Fig. 7 Two cross sections of Fig. 5 measured at position at the center of the shocked line, and at unshocked position (100 μm away from the shocked line center)

shock peening, the X-ray profile was significantly broadened and became asymmetric compared to unshocked region for both (001) and (110) samples. Considering the X-ray profile of (001) sample at 5 μm right of the shocked line center as shown in details in Fig. 9, the raw profile represented by the unsmoothed curve is smoothed to obtain the fitted profile I , which is subsequently decomposed into two symmetric sub profiles I_c and I_w using Lorentzian peak function^[26]. The centers

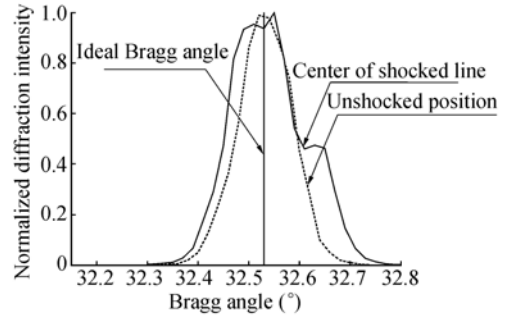


Fig. 8 Two cross sections of Fig. 6 measured at position at the center of the shocked line, and at unshocked position (100 μm away from the shocked line center)

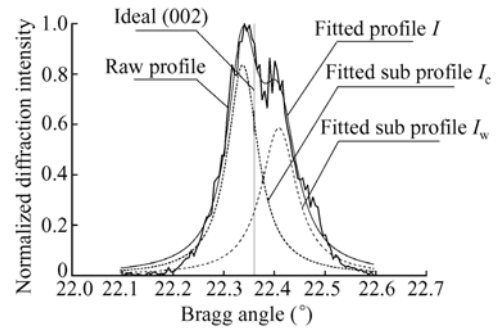


Fig. 9 Detailed view of decomposition of an asymmetric line profile into the sum of two symmetric sub-profiles, diffraction intensity normalized (Sub profile I_c , cell interior; and Sub profile I_w , cell wall)

of the decomposed sub-profiles are found to be shifted in opposite directions and the shifts can be related to the relative change of the mean lattice plane spacing $\Delta d / d$ of the corresponding lattice planes

$$\left. \frac{\Delta d}{d} \right|_{c(or w)} = -\cot \theta \Delta \theta_{c(or w)} \quad (8)$$

where $\Delta \theta_{c(or w)}$ is the angular shift of the sub-profiles I_c (or I_w) relative to the exact Bragg angle θ of the shock free regions. This equation is based on taking total differential of the Bragg law assuming perfect X-ray wavelength. For Al (002) reflection profile at position +5 μm from the shocked line, the ideal Bragg angle corresponding to the shocked free regions is $\theta = 22.36^\circ$, the centers of gravity of the decomposed sub-profiles are $\theta_c = 22.328^\circ$ and $\theta_w = 22.388^\circ$, and therefore, $\Delta \theta_c = -0.032^\circ$ and $\Delta \theta_w = 0.028^\circ$. For Al crystals with $E = 70$ GPa and $\nu = 0.33$, $\Delta \sigma_c$ and $\Delta \sigma_w$ are 95 MPa and -82.6 MPa according to Eqs. (2) and (8). Equation (3) gives the axial residual stress $\sigma_{zz} = 177.6$ MPa and Eq. (4) gives the lateral residual stress within the sample surface plane as:

$$\sigma_{xx} = \sigma_{yy} = -\sigma_{zz} = \nu = -58.6 \text{ MPa} \quad (9)$$

The volume fractions f_w and f_c of the walls and cell interiors can be obtained from the fractional integral intensities of the sub-profiles relative to the integral intensity of the total profile. Following the analysis method above for each measurement point, the spatially resolved residual stress distribution for Al (001) is shown in Fig. 10. The simulation results from FEM are also overlapped in Fig. 10. The distributions show similar patterns and generally agree with each other. In terms of the lateral extent of the compressive residual stress, the experiment results give around $\pm 30 \mu\text{m}$ from the center of shocked line, while the FEM results overestimate it. This is likely due to the shock pressure model used in the FEM which may have overestimated the lateral expansion effect of pressure loading on the sample surface^[4].

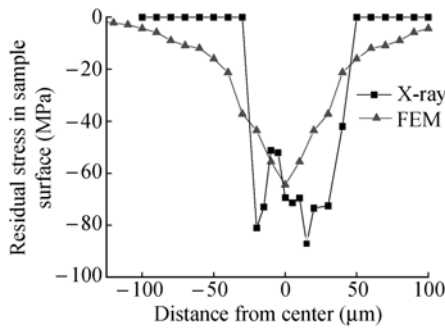


Fig. 10 Typical spatial distribution of residual stress in Al (001) sample surface by X-ray diffraction measurement and FEM simulation

3.1.2 Strain deviation spatial distribution across the shocked region

To better understand the shock-induced plastic deformation, it is necessary to study the corresponding inhomogeneous strain variation in the depth direction, which can be calculated from the recorded X-ray profiles according to the method discussed in Section 2.4. From the theory of Ref. [23], for small values of l and n , the logarithm of the measured Fourier coefficient is given by Eq. (7). For Al (002) reflection, $l = 2$, so the strain effect term can be represented as $-2\pi^2 l^2 n^2 \langle \varepsilon_l^2 \rangle^{1/2}$, in which $\langle \varepsilon_l^2 \rangle^{1/2}$ represented standard strain deviation caused by the laser shock peening in the [002] direction, which is in the depth direction perpendicular to the surface for Al(001) sample. If we choose n^2 as the x -axis and $\ln A_n(l)$ as the y -axis, Eq. (7) represents a straight line with slope $K = -2\pi^2 l^2 \langle \varepsilon^2 \rangle$. Thus, the

slope of this fitted line can be used to calculate the strain deviation from that X-ray profile as

$$\langle \varepsilon_l^2 \rangle^{1/2} = \sqrt{\frac{K}{-2\pi^2 l^2}} \quad (10)$$

For example, at the position (10 μm) from the shocked line, the slope of fitted line is $K = -0.05035$, $l = 2$ for Al (002) reflection, so the $\langle \varepsilon_l^2 \rangle^{1/2}$ is 0.025 based on Eq. (10). In order to obtain the spatial distribution of the strain deviation in depth direction, X-ray profiles at each position cross the shocked line (from 30 μm left of the shocked line to 30 μm right) were processed by using Fourier transformation with Stoke's correction^[26]. Fourier number n^2 vs. $\ln A_n$ for sample Al (001) was shown in Fig. 11^[27]. It is clear that the magnitude of line slope increases from the position far away from the shocked line center (30 μm) to the center of shocked line (0 μm). It shows that the strain deviation increases gradually when the position moves closer to the shocked center. Figure 12 shows the spatial distribution of strain deviation in depth for Al (001) sample by Fourier analysis. For the FEM

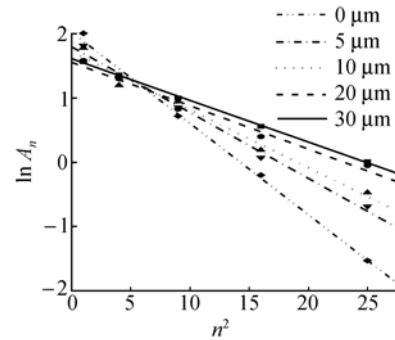


Fig. 11 $\ln A_n$ vs. n^2 lines at different positions from the center of the shocked line for Al (002) reflection^[27] (A_n is the real part of corrected Fourier coefficient and n is Fourier series number)

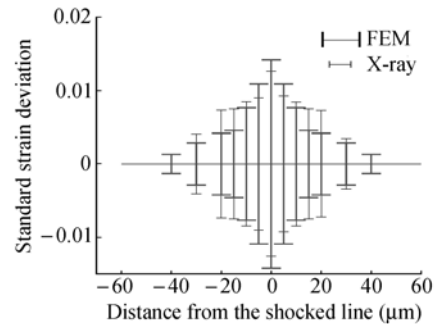


Fig. 12 Standard strain deviation in depth direction by Fourier transformation and FEM simulation for sample (001)

simulation, the corresponding standard strain deviation at each point can be obtained through a surface layer of effective depth of X-ray penetration. Arbitrarily choosing the depth of 90% of the total diffracted intensity

$$\text{Depth} = \frac{2.3 \sin \theta_0}{2\mu} \quad (11)$$

where θ_0 is ideal Bragg angle, μ is the linear absorption coefficient, and the effective depth is $45 \mu\text{m}$ for single crystal aluminum (110) with $\theta_0=32.53$ and $\mu=135.6 \text{ cm}^{-1}$ [17]. In this surface layer of depth $45 \mu\text{m}$, nine values of strain can be obtained if spacing is $5 \mu\text{m}$ in depth direction at each point. Thus, the standard strain deviation for the FEM simulation is

$$\text{SD} = \sqrt{\frac{\sum_{i=1}^m (\varepsilon_i - \bar{\varepsilon})^2}{m-1}} \quad (12)$$

where m is the sample size, $\bar{\varepsilon}$ is the average strain at each point. As seen in the Fig. 12, the maximum strain deviation levels can be found in a region of $\pm 20 \mu\text{m}$ from Fourier analysis of X-ray profile which is in good agreement with the result from the FEM simulation.

3.2 Microscopic quantities

3.2.1 Crystal lattice rotation

Crystal lattice rotation is well-defined within the context of kinematics of single crystal plasticity and a key parameter in simulation model. It is well known that both face-centered cubic (FCC) and body-centered cubic (BCC) crystals admit a state of plane strain deformation if the crystal is oriented and the mechanical loading is applied along certain crystallographic directions[28]. The current orientation of the lattice directions with respect to the initial one is determined by the rotation in the polar decomposition of the elastic part of deformation[29]. Therefore, crystalline orientation field measured from EBSD enables characterization of the in-plane lattice rotation induced by micro-scale laser shock peening under approximate plane strain conditions to be compared with the results from the FEM analysis.

The lattice rotation contour map on the shocked Al (001) sample's surface is shown in Fig. 13a. Figure 13b shows the spatial distribution of lattice rotation along two lines across the shocked line with $34 \mu\text{m}$ spacing. Region 1 corresponds to counter-clockwise rotation about the z -axis which is positive and Region 2

corresponds to clockwise rotation which is negative. It is clear to see that the lattice rotation is zero far away from the shocked line which corresponds to the shock free region. The lattice rotation distribution along the shocked line is quite similar along two lines which suggest the approximate two-dimensional deformation state. The lattice rotation value is $\pm 3^\circ$ between $\pm 35 \mu\text{m}$ from the center of the shocked line and the rotation direction is anti-symmetric on both sides of the shocked line. In order to investigate the effect of crystal orientation on lattice rotation, an aluminum sample shocked on the (110) surface was also studied as seen in Figs. 14a and 14b. The general trend of lattice rotation, such as the rotation direction and magnitude, is the same with that of Al (001).

The simulation for the spatial distribution of the lattice rotation was carried out and shown in Fig. 15. It can be seen that the lattice rotation distribution is quite similar with the experimental results. When the position changes from the left of the shocked line to the right for Al (011), the lattice rotation starts from zero degree (beyond $\pm 40 \mu\text{m}$) to maximum negative value (-4° at $-15 \mu\text{m}$) and after that, the magnitude of

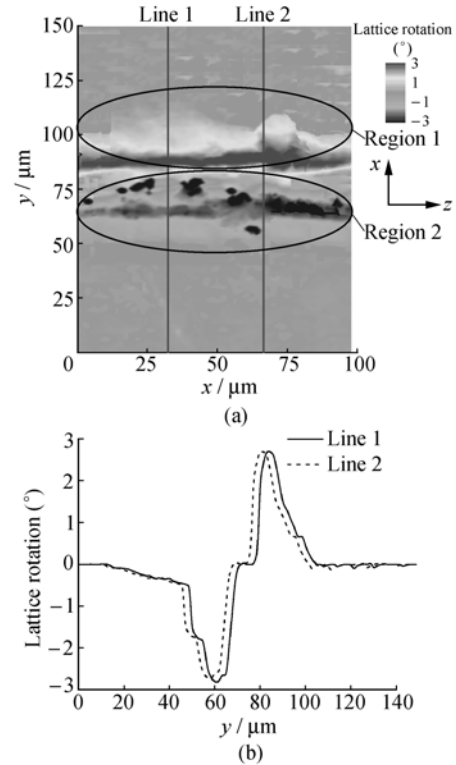


Fig. 13 Lattice rotation contour map on sample surface for Al (001) sample (Lines 1 and 2: two cross sections with spacing = $34 \mu\text{m}$)

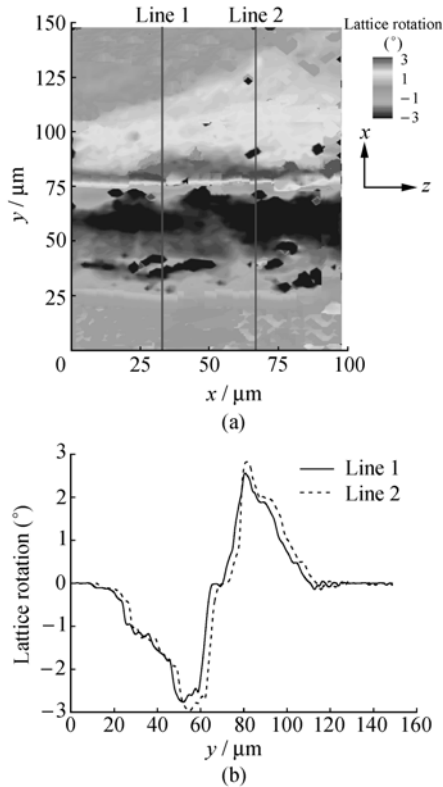


Fig. 14 Lattice rotation contour map on sample surface for Al (110) sample (Lines 1 and 2: two cross sections with spacing = 34 μm)

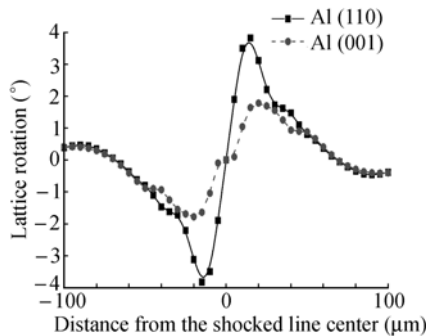


Fig. 15 Spatially distribution of the lattice rotation on the sample surface from the simulation

lattice rotation decreases to zero again close to the shocked line center. For the right side of the shocked line center, the distribution is anti-symmetric with the left side.

3.2.2 Average mosaic size

Size broadening effect is represented by a cosine Fourier series similar to that developed for strain broadening and hence the Fourier coefficients A_n give very general method of handling either effect. From the analysis of Ref. [23], the initial slope of the A_n vs. n

curve is

$$\left(\frac{dA_n}{dn}\right)_{n=0} = -\frac{1}{\bar{N}_3} \tag{13}$$

where \bar{N}_3 is the average number of cells per column. Hence the average column length is $\bar{N}_3 a_3$ if assuming a_3 is the crystal lattice constant in normal direction. Also, we have

$$1/2 = (2a_3 / \lambda)(\sin \theta - \sin \theta_0) \tag{14}$$

where λ is the wavelength of X-ray, θ is the maximum angle in X-ray profile, and θ_0 is the ideal Bragg angle. So if the size broadening effect is expressed in terms of a plot of the Fourier coefficients A_n vs. n , the initial slope of the curve gives directly the average column length, which is the average mosaic size in that direction.

Figure 16 shows the initial slope of the A_n vs. n curve (the line connecting the first two points in A_n - n curve) at different distances from the shocked line center. If the initial slope of curve is K , then the average mosaic size D at that position can be evaluated as

$$D = \frac{1}{K} \square a_3 \tag{15}$$

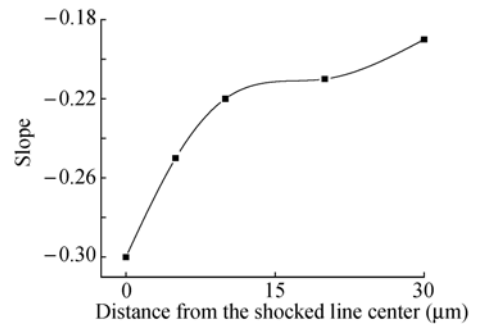


Fig. 16 Initial slope of A_n vs. n curves for Al (110) sample

From the analysis above, the size effect can be obtained from Fourier analysis of X-ray profiles. Figure 17 shows the spatial distribution of the average mosaic size for Al (110) sample evaluated from the X-ray profile analysis mentioned above. It can be seen that the average mosaic size decreases when it moves closer to the shocked line center. In the region of $\pm 20 \mu\text{m}$ from the center, the mosaic size is around $1 \mu\text{m}$ to $0.7 \mu\text{m}$ and increases sharply to over $100 \mu\text{m}$ beyond this range. This is reasonable since the shock peening effect is higher in the shocked line center and larger plastic deformation will favor the formation of mosaic structure.

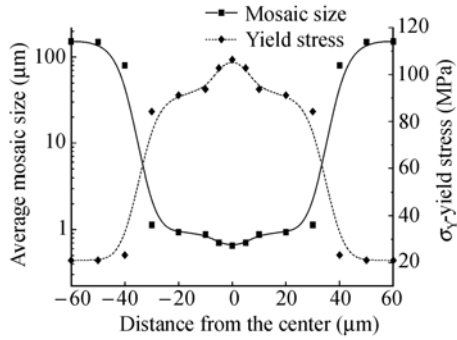


Fig. 17 Spatial distribution of average mosaic size from initial slope analysis by the fast Fourier transform and shock-induced strengthening effects for Al (110)

In addition to using X-ray profile analysis to obtain the mosaic size distribution after laser shock peening, EBSD measurement was also applied to sample (110) surface and mosaic structure can be studied directly and compared with the result from X-ray. Mosaic structures can be quantitatively analyzed through EBSD measurements because EBSD is based on data acquisition of crystalline misorientation angles with sub-micron spatial accuracy, and the misorientation angle accuracy is less than 1°. Figure 18a shows the microstructures of mosaic for Al (110) sample. The thin lines show mosaic boundaries whose misorientation angles are larger than 3°. The line *L* represents laser shocked line. The cross sections represented by Lines 1, 2 and 3 with spacing 12.5 μm are made perpendicular to the shocked line. The spatial distribution of mosaic size along the three lines is shown in Fig. 18b. It is observed that within the shock peening region (±20 μm from the shocked line center), it has a larger increase in mosaic structure and the smallest mosaic size of 0.8 μm dominant in the center and become larger away from the shock peened region. The result is consistent with the result obtained from the X-ray profile analysis mentioned above.

As a result of a mosaic size refinement, the shocked area is strengthened according to well-known empirical relationship such as the Hall-Petch relation between average grain size and the yielding limit of a bulk metal^[30] since metal in shocked area can be considered as polycrystalline metal due to the mosaic structure

$$\sigma_Y = \sigma_0 + \frac{k}{\sqrt{D}} \quad (16)$$

where σ_Y is the flow stress, k is the material dependent

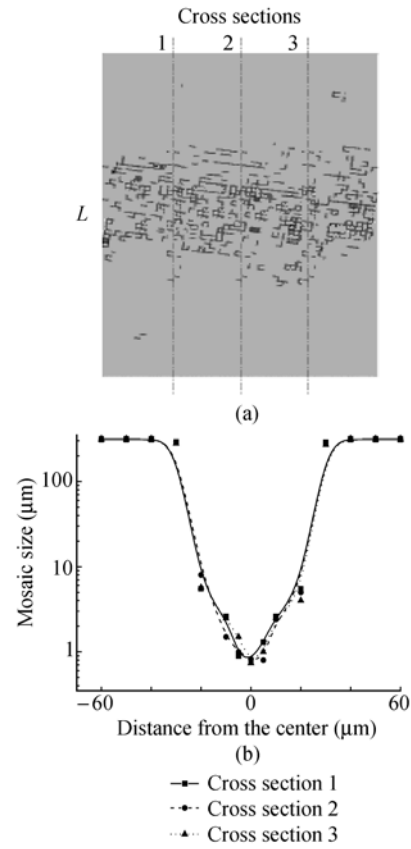


Fig. 18 Mosaic microstructure distribution of Al (110) sample on shocked peened surface measured with EBSD (50 μm×80 μm). Three cross sections perpendicular to the shocked line are indicated by 1, 2 and 3^[27].

constant, and D is the average mosaic size. For pure aluminum (99.99%), the corresponding σ_0 and k are $\sigma_0 = 15$ MPa and $k = 2.33$ MPa√mm^{1/2}^[30]. The yield stress spatial distribution across the shocked area can be obtained by using the average mosaic size and is shown in Fig. 17. It can be seen that strength is improved significantly in the shocked area and the yield stress is increased to almost 110 MPa in the shocked line center by microlaser shock peening.

Other than the method of Fourier analysis, average mosaic size can also be roughly estimated by the Scherrer formula^[17]:

$$D = \frac{0.9\lambda}{B \cos \theta_0} \quad (17)$$

where λ is the wavelength, B is the broadening of diffraction line measured at half its maximum intensity (radians), and θ_0 is the ideal Bragg angle. By using the X-ray profile at 100 μm from the shocked line to correct the instrumental broadening, the calculated

average mosaic size is shown in Fig. 19, which shows that the mosaic size is much smaller than the result by the Fourier analysis, because X-ray line broadening is related to the sample and instrument. Sample broadening is usually from mosaic size and inhomogeneous strain variation in the spacing along the normal direction. The method of the Scherrer formula considers that the total X-ray profile broadening is only caused by the small mosaic size, while Fourier analysis separates the total broadening effect into two parts and calculates mosaic size and strain deviation, respectively. Thus, compared to the result from Fourier analysis, mosaic size of the Scherrer formula is smaller. Therefore, Fourier analysis should be used to precisely calculate mosaic size from the recorded X-ray profiles.

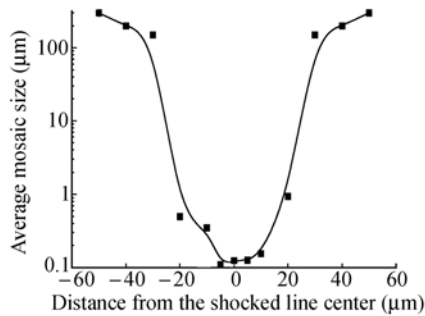


Fig. 19 Spatial distribution of the average mosaic size calculated by the Scherrer formula for Al (110)

3.3 Further understanding of dislocation cell structure

The recorded X-ray profile for the single crystal Al samples (Figs. 5 and 6) strongly suggests the existence of dislocation cell structure. In fact, dislocation cell structures were observed via transmission electron microscopy (TEM) in laser shock peened metals, such as copper^[31]. This accompanies the generation and storage of a larger dislocation density during the shock process than for quasi-static processes.

There are various models of dislocation patterning. According to the thermodynamic approach, dislocation cells are considered as low-energy structures^[32]. This approach is, however, incorrect as energy minimization principles do not apply to dissipative processes far from equilibrium, such as dislocation glide during plastic deformation. In the synergetic theories developed by Ref. [33], the nonlinear dynamics of various dislocation densities is considered, such as mobile, immobile, and dipole dislocation configurations and

the evolution and dynamic stability of dipolar dislocation arrangements are mainly concerned. An inherent weakness of this model relates to the neglect of long-range dislocation interactions. This could be a problem with dislocation cell formation where patterning occurs at the same mesoscopic length scale that governs the effective range of dislocation interactions.

In another model, it is assumed that the geometrically necessary effective stress fluctuations experienced by gliding dislocations cause appreciable fluctuations of the local strain rate. This enables the mobile dislocations to probe again and again new configurations. During this process, energetically favorable configurations possess a certain chance to become stabilized, whereas unfavorable arrangements are rapidly dissolved again. While cross slip supports this process by increasing the “selection pressure”. That is, through the range increase of possible slip planes, cross-slip increases the efficiency with which dislocations can move down energy gradients. Based on the stochastic dislocation dynamics model from Ref. [34], cross slip will increase the fraction of mobile dislocations so the dislocation cell formation is favored by easy cross slip. Figures 5 and 6 show 3-D Bragg reflection profiles along the direction cross the shocked line for Al (001) and Al (110) samples. The asymmetric line profile is significant mainly in the range of $\pm 20 \mu\text{m}$ from the shocked line center for (110) orientation compared to the $\pm 30 \mu\text{m}$ range in (001) orientation. Also as shown in Fig. 20, the volume of cell wall is less in (110) orientation and has narrower spatial distribution. So, the (001) orientation is easier to form dislocation cell structure than (110) orientation in microscale laser shock peening. As shown in Fig. 21, it is well known for FCC crystal that the plastic slip systems are the $\{111\}$ family of planes in the $\langle 110 \rangle$ family of directions, for a total of 12 possible slip systems. However, the distribution of the resolved shear stress in each slip system for loading in different orientation is different^[35]. The slip systems which have maximum resolved shear stresses for loading applied in (001) and (110) orientation samples are shown below and slip would occur in those slip systems. For the (110) orientation, there are 4 possible activated slip systems $(111)[10\bar{1}]$, $(111)[0\bar{1}1]$, $(\bar{1}\bar{1}1)[011]$, and $(\bar{1}\bar{1}1)[101]$. For the (001) orientation, there are 8 possible activated slip systems: $(111)[10\bar{1}]$, $(111)[1\bar{1}0]$,

$(\bar{1}\bar{1}\bar{1})$ $[10\bar{1}]$, $(\bar{1}\bar{1}\bar{1})$ $[110]$, $(1\bar{1}\bar{1})$ $[110]$, $(1\bar{1}\bar{1})$ $[101]$, $(\bar{1}\bar{1}\bar{1})$ $[101]$, and $(\bar{1}\bar{1}\bar{1})$ $[1\bar{1}0]$. As a result, for the (110) orientation, cross slip is more difficult to occur since there is no common slip direction between different slip planes. However, in the (001) orientation, the slip systems $(111)\langle 10\bar{1}\rangle$ and $(\bar{1}\bar{1}\bar{1})\langle 10\bar{1}\rangle$ can generate the cross slip between these two slip planes. For the total eight slip systems, cross slip can occur between every two of them. Thus, the cross slip is much easier to occur in (001) orientation than in (110) orientation and this favors the formation of cell structure in (001) orientation.

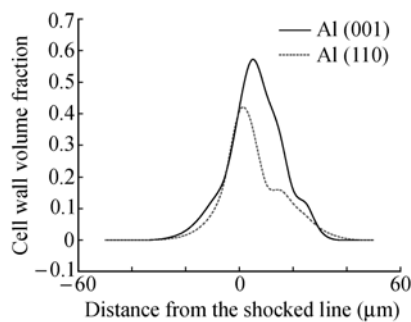


Fig. 20 Volume fraction of cell wall at each measure point for Al (001) and (110)

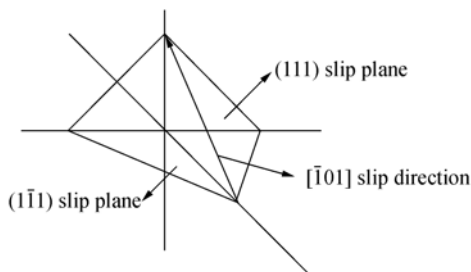


Fig. 21 Cross slip formation in FCC metal, (111) planes in the $\langle 110 \rangle$ direction

4 Conclusions

The FEM simulation results and experimental characterization method presented herein enable a systematic study of the microscale laser shock peening process. The resolved spatial residual stress/strain distribution was achieved in micron-level by X-ray microdiffraction.

The compressive residual stress is -80 MPa to -100 MPa within ± 20 μm from the shocked line center and it decreases very quickly to a few MPa beyond that range. Crystal orientation (001) was found to be more beneficial to the formation of cell structure than the (110) orientation. Also, strain deviation at the depth

direction and the average mosaic size was extracted from the recorded X-ray profiles. The lattice rotation field was found to be anti-symmetric on the surface across the shocked line. The magnitude of rotation is $\pm 3^\circ$ and covers a region around ± 35 μm across the shocked line center. Mosaic-like substructure was formed in submicron size within the region ± 20 μm from the shocked line center and consistent with the measurement from EBSD. Strength of peened region was increased due to the mosaic structure. The experimental results were compared with that from the FEM analysis and the results show a close correspondence between them. Both the results from experiments and the FEM analysis indicate that the microscale laser shock peening induces very localized effects, such as in micron-level. Thus, this technique can be used to improve the reliability performance of microdevices and the process can be optimized with the above systematic study.

Acknowledgement

Guidance in X-ray microdiffraction provided by Dr. I. Cev Noyan and Dr. Jean Jordan-Sweet is appreciated. Assistance in technique details in sample preparation for EBSD provided by Dr. Yongxue Gang and Mr. J. B. Chou is also acknowledged.

References

- [1] Walraven J A, Mani S S, Fleming J G, Headley T J, Kotula P G, Pimentel A A, Rye M J, Tanner D M, Smith N F. Failure analysis of tungsten coated polysilicon micro-machined microengines. *MEMS Reliability for Critical Applications, Proceedings of SPIE*, 2000, **4180**: 49-57.
- [2] Frederick K M, Fedder G K. Mechanical effects of fatigue and charge on CMOS MEMS. *MEMS Reliability for Critical Applications, Proceedings of SPIE*, 2000, **4180**: 108-116.
- [3] Zhang W, Yao Y L. Feasibility study of inducing desirable residual stress distribution in laser micromachining. In: Transactions of the North American Manufacturing Research Institution of SME (NAMRC XXIX) 2001, 2001: 413-420.
- [4] Zhang W, Yao Y L. Improvement of laser induced residual stress distributions via shock waves. *Proc. ICALEO'00, Laser Materials Processing*, 2000, **89**: E183-192.
- [5] Zhang W, Yao Y L. Micro scale laser shock processing of metallic components. *ASME Journal of Manufacturing Science and Engineering*, 2000, **124**(2): 369-378.
- [6] Chen H Q, Yao Y L. Modeling schemes, transiency, and strain measurement for microscale laser shock processing.

- In: Trans. of the North American Manufacturing Research Institution of SME, NAMRC 31. Canada: Hamilton, May 20-24, 2003: 589-596.
- [7] Noyan I C, Jordan-Sweet J L, Liniger E G, Kaldor S K. Characterization of substrate/thin-film interfaces with X-ray microdiffraction. *Applied Physics Letters*, 1998, **72**(25): 3338-3340.
- [8] Noyan I C, Wang P C, Kaldor S K, Jordan-Sweet J L. Deformation field in single-crystal semiconductor substrates caused by metallization features. *Applied Physics Letters*, 1999, **74**(16): 2352-2354.
- [9] Hutchinson J W. Plasticity at the micron scale. *International Journal of Solids and Structures*, 2000, **37**: 225-238.
- [10] Clauer A H, Fairland B P. Interaction of laser-Induced stress waves with metals. *Highway Engineer*, 1979: 291-315.
- [11] Nalla R K, Altenberger I, Noster U, Liu G Y, Scholtes B, Ritchie R O. On the influence of mechanical surface treatments deep rolling and laser shock peening on the fatigue behavior of Ti-6Al-4V at ambient and elevated temperatures. *Materials Science and Engineering*, 2003, **A355**: 216-230.
- [12] Fabbro R, Fournier J, Ballard P, Devaux D, Virmont J. Physical study of laser-produced plasma in confined geometry. *J. Appl. Phys.*, 1990, **68**(2): 775-784.
- [13] Asaro R J. Micromechanics of crystals and polycrystals. *Advances in Applied Mechanics*, 1983, **23**: 1-115.
- [14] Huang Y. A user-material subroutine incorporating single crystal plasticity in the ABAQUS finite element program. Mech Report 178. Division of Applied Sciences, Harvard University, Cambridge, MA, 1991.
- [15] Kysar J W. Addendum to "A user-material subroutine incorporating single crystal plasticity in the ABAQUS finite element program, Mech Report 178". Division of Engineering and Applied Sciences, Harvard University, Cambridge, MA, 1997.
- [16] ABAQUS/Standard User's Manual, Version 6.2. Hibbit, Karlsson and Sorensen, Inc., Pawtucket, RI, USA, 2002.
- [17] Cullity B D. Elements of X-ray Diffraction, Second Edition. London: Addison-Wesley Publishing Company, Inc., 1978: 268-270.
- [18] Noyan I C, Wang P C, Kaldor S K, Jordan-Sweet J L. Divergence effects in monochromatic X-ray microdiffraction using tapered capillary optics. *Review of Scientific Instruments*, 2000, **71**(5): 1991-2000.
- [19] SPECTM X-ray diffraction software. Certified Scientific Software, Cambridge, MA, 2000.
- [20] HKL Channel 5TM User's Manual. HKL Technology, Danbury, CT, 2001.
- [21] Chen H Q, Kysar J W, Yao Y L. Characterization of plastic deformation induced by micro scale laser shock peening. *ASME Journal of Applied Mechanics*, 2003. (in Press)
- [22] Ungar T, Ribarik G, Gubicza J, Hanuk P. X-ray line-broadening study of the dislocation cell structure in deformed [001]-orientated copper single crystals. *Acta Metall.*, 1984, **32**(3): 332-342.
- [23] Warren B E, Averbach B L. The effect of cold-work distortion on X-ray patterns. *Journal of Applied Physics*, 1950, **21**: 595-599.
- [24] Chen H Q, Yao Y L, Kysar J W. Spatially resolved characterization of residual stress induced by micro scale laser shock peening. In: Proc. of 22nd International Congress on Applications of Lasers & Electro-Optics (ICALEO). Conference on Laser Materials Processing, Section B. Jacksonville, FL, October 13-16, 2003: 1-10.
- [25] Warren B E. X-ray Diffraction. Addison-Wesley, Reading, MA, 1969.
- [26] Noyan I C, Cohen J B. Residual Stress-Measurement by Diffraction and Interpretation. New York: Springer-Verlag Inc., 1987: 168-175.
- [27] Chen H Q, Yao Y L, Kysar J W, Noyan I C, Wang Y N. Fourier analysis of X-ray microdiffraction profiles to characterize laser shock peened metals. In: The North American Manufacturing Research Institution of SME, NAMRC 32. Charlotte, NC, June 1-4, 2003.
- [28] Rice J R. Tensile crack tip fields in elastic-ideally plastic crystals. *Mechanics of Materials*, 1987, **6**(4): 317-335.
- [29] Mandel J. Definition of a frame suitable to the study of anelastic transformations of polycrystal. *Journal de Mécanique Théorique et Appliquée*, 1982, **1**(1): 7-23.
- [30] Meyers M A, Armstrong R W, Kirchner H. Mechanics and Materials: Fundamentals and Linkages. New York: John Wiley & Sons, Inc., 1999: 377-381.
- [31] Murr L E. Microstructure-Mechanical Property Relations, Shock-Wave and High-Strain-Rate Phenomena in Metals. New York: Plenum Press, Inc., 1981: 607-671.
- [32] Hansen N, Kuhlmann-Wilsdorf D. Proceedings of the international conference on low-energy dislocation structures. *Materials Science and Engineering*, 1986, **81**: 141-152.
- [33] Kratochvil J. Instability origin of dislocation cell misorientation. *Scripta Metallurgica et Materialia*, 1990, **24**(7): 1225-1228.
- [34] Hahner P. A theory of dislocation cell formation based on stochastic dislocation dynamics. *Acta Mater.*, 1996, **44**(6): 2345-2352.
- [35] Stouffer D C, Dame L T. Inelastic Deformation of Metals. New York: John Wiley & Sons, Inc., 1996: 12-15.